PHYSICAL REVIEW A **85**, 033827 (2012)

Near-field mapping of optical eigenstates in coupled disk microresonators

C. Schmidt,[1,*] M. Liebsch,[1] A. Klein,[1] N. Janunts,[1] A. Chipouline,[1] T. Käsebier,[1] C. Etrich,[2] F. Lederer,[2] E.-B. Kley,[1]
A. Tünnermann,[1,†] and T. Pertsch[1]
[1]*Institute of Applied Physics, Abbe Center of Photonics, Friedrich-Schiller-Universität Jena, Max-Wien-Platz 1, 07743 Jena, Germany*
[2]*Institute for Condensed Matter Theory and Solid State Optics, Abbe Center of Photonics, Friedrich-Schiller-Universität Jena,*
Max-Wien-Platz 1, 07743 Jena, Germany

(Received 17 November 2011; published 22 March 2012)

We report on the real-space experimental observation of whispering-gallery modes in coupled disk microresonators excited by a tapered optical fiber. Using a high-resolution scattering scanning near-field optical microscope (SNOM) technique, the resonator modes can be perturbed, leading to altered transmission and reflection through the tapered fiber. The correlation of the perturbed signals with the position of the perturbing SNOM tip results in intensity maps of the optical resonator modes under investigation. A combination of a coupled-mode theory of the excited microresonator including the SNOM tip and a two-dimensional modal expansion technique can be used to understand different regimes of the perturbation, leading to qualitatively different transmission and reflection maps for the same optical resonator mode. Detailed measurements of the intensity distributions of eigenmodes of two and three coupled disks in different arrangements are presented and compared to theoretical calculations.

DOI: 10.1103/PhysRevA.85.033827 PACS number(s): 42.25.Bs, 42.50.Ct, 42.60.Da, 42.82.Et

I. INTRODUCTION

Coupled optical microresonators have been attracting considerable attention in recent years. A combination of the advantageous properties of single microresonators [1,2] with the evanescent coupling by placing such resonators very close to each other results in systems of specific properties. For a few coupled resonators, effects like electromagnetically induced transparency [3], slow light [4], and optical bistability [5,6] were observed. The coupling of a larger number of resonators forms a new class of optical waveguides, namely, coupled resonator optical waveguides (CROW [7]), which can be used, for example, as optical delay lines [8] and high-order filters [9,10]. Extending the coupling of the resonators to two-dimensional arrays allows the formation of photonic molecules [11], which can be used as optical sensors [12] or active lasing elements [13,14].

Especially for sensor applications (e.g., nanoparticle detection [15]), which are based on a resonance shift due to the interaction of a nanoparticle with the cavity mode, the mode's intensity distribution is of particular interest. Due to the different spatial distributions of excited modes in coupled arrays of microresonators, it is possible to constrain the position of the perturbation across the array just by looking at changes in the spectrum. Motivated by this, we implemented a high-resolution mode mapping technique for coupled microdisks using a scattering scanning near-field optical microscope (SNOM) tip for perturbation of the eigenmodes of the system. By recording the changes in transmission and reflection through a tapered fiber used for excitation of the coupled resonators depending on the position of the tip, the intensity distribution of the modes can be mapped. The measurement principle is adapted from waveguide mode mapping [16], as well as investigations of eigenmodes in photonic crystal cavities [17]. Previous methods for visualization of the mode distribution of on-chip microresonators include the far-field observation due to the collection of out-of-plane scattering [18], up-conversion in erbium-doped microresonators [19], and the near-field mapping of single microdisks by direct collection with an aperture SNOM [20] or by a scattering SNOM technique collecting the scattered light from the tip in the far field [21].

In addition to the experimental studies presented here, theoretical calculations are of importance to identify different regimes of the interaction between the scatterer and the excited cavity system. To obtain fast and reliable calculations, a combination of two different approaches was used to address the important parts of the experimental system. First is the waveguide-resonator coupling, which can be modeled using coupled-mode theory [22] and taking into account the coupling of the scattering SNOM tip to the whispering-gallery mode (WGM) of the microresonator, which can be described in a semiquantum optical framework [23]. Second is the calculation of the field distribution in arbitrarily coupled microresonators using a rigorous two-dimensional modal expansion method [12].

The paper is organized as follows. In Sec. II, we introduce the coupled microresonator system and the measurement principle. In Sec. III, we describe the theoretical model that was used to understand the observed transmission and reflection signals for different regimes of perturbation by the SNOM tip. We characterize the measured signals in general in Sec. IV and test the model for the case of a single disk to identify the influences of the SNOM tip in detail. In Sec. V, we present detailed results of eigenmode mappings of two coupled disks and three coupled disks in different configurations.

II. COUPLED MICRORESONATOR SYSTEM AND MEASUREMENT PRINCIPLE

The system of coupled microresonators under investigation consists of freestanding fused silica microdisks on a silicon

---

[*] ca.schmidt@uni-jena.de

[†] Also at: Fraunhofer Institute of Applied Optics and Precision Engineering, Jena, Germany.

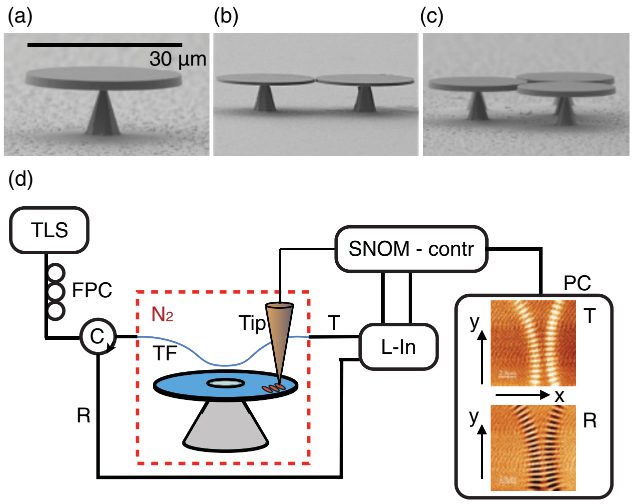

FIG. 1. (Color online) Different samples under investigation: (a) single disk, (b) two coupled disks, and (c) three coupled disks in a triangular configuration (linear arrangement not shown). (d) A sketch of the setup showing the tunable laser source (TLS, with modulation for lock-in), a fiber polarization controller (FPC), and a circulator (C) for extraction of the reflection signal (R). The sample, the tapered fiber (TF), and the SNOM tip (Tip) are placed in a nitrogen-purged box. The reflection and transmission (T) signals are fed into a lock-in amplifier (L-In) with the amplitude outputs connected to the SNOM controller (SNOM-contr) where the signals are correlated to the position of the tip. A PC is used to control all devices and to read out the measured transmission and reflection mode maps.

chip. A detailed description of the fabrication process can be found in Refs. [6,24]. For the presented analysis, we used a single disk sample, two coupled disks, and three coupled disks in a line and in a triangular arrangement (see Fig. 1). All disks in all samples have a diameter of about 30 μm and a thickness of 1 μm. The gap size between the coupled disks is in the range of 300 to 500 nm, which is sufficient to observe optical coupling for the measured wavelength range around 1550 nm. The samples were placed in a nitrogen-purged box to prevent them from contamination and air flow in the laboratory environment. For the optical excitation, a tapered optical fiber was used to couple light from a tunable laser source (Agilent 81600/81640A) to one of the disks of the sample. In parallel, the tapered fiber was used to collect the transmission and reflection signal modified by the spectral response of the sample, and the signals were detected by photoreceivers (Terahertz Technology Inc. TIA-525I). By tuning the pump laser over a certain wavelength range (1510 to 1570 nm), the resonance wavelengths of the sample can be determined. For the mode mapping experiments, the pump laser wavelength was fixed to one of the resonances, which results in a certain transmission and reflection value. The apertureless tip of a scanning near-field optical microscope (MV4000, Nanonics Imaging Ltd.) was placed above the disk sample and scanned across the surface in tapping mode. When the SNOM tip (gold coated, diameter 50 to 100 nm) reaches the rim of the disk, where the excited WGM is located, it can interact with the mode's near field. The presence of the tip (its polarizability) changes the effective refractive index of the environment, which has influences on the resonance condition and leads to a shift of the mode's resonance wavelength. Additionally, to this induced effective refractive index change, the tip also acts as a scatterer. This can lead to coupling of photons of the excited mode to either radiation modes (reservoir modes) or to other WGMs, which have spectral and spatial overlap with the excited mode. The only mode which matches the latter conditions for the samples under investigation is the mode counterpropagating to the excited WGM. This leads to a coupling-induced splitting of the resonance in the spectrum, which is observable when it is larger than the mode's bandwidth. On the other hand, the coupling to the radiation modes, which is an additional loss channel, leads to a broadening of the resonance and a signal reduction. Both effects therefore have influences on the transmission and reflection values depending on the strength of the interaction of the mode with the tip. When correlating the measured signals with the position of the tip using the SNOM controller, a map of the near-field interaction strength can be obtained, which is actually an intensity map of the mode due to the fact that the interaction strength depends on the field intensity at the position of the tip. To increase the signal-to-noise ratio, a lock-in amplification scheme was used. It is worth noting that the implemented lock-in technique is not essential to get reasonable results, which underlines the sensitivity of the described method in comparison to scattering into far-field SNOM methods [21].

III. THEORETICAL MODEL

The interaction of the SNOM tip with the modes of the microdisk resonator as well as the signal collection through the tapered fiber have a strong effect on the appearance of the measured signals. However, we are not interested in the response of the whole system, but only in the mode distribution of the coupled microdisks. Therefore, we combine the calculation of the intensity distribution of coupled microdisks with a coupled-mode theory, taking into account the SNOM tip and the tapered fiber coupling in order to calculate reflection and transmission signals, which can be compared to the measured data. From this, a link from the measured signals to the intensity distribution of the mode of the coupled microdisk sample is possible.

A. Field distribution in coupled microdisks

The system of coupled disk microresonators studied in this paper can be described in the framework of a two-dimensional modal expansion. Based on the detailed description in Ref. [18], the internal (int), scattered (sc), and incident (inc) fields can be written as a linear combination of cylindrical harmonics [Bessel (Hankel) function inside (outside) of the disks],

$$F_{\text{int}}^{(p)} = \sum_m d_m^{(p)}(\omega) e^{im\phi_p} J_m(n_{\text{d}} k |\mathbf{r} - \mathbf{r}_p|), \tag{1}$$

$$F_{\text{sc}}^{(p)} = \sum_m b_m^{(p)}(\omega) e^{im\phi_p} H_m(n_0 k |\mathbf{r} - \mathbf{r}_p|), \tag{2}$$

$$F_{\text{inc}}^{(p)} = \sum_m \Bigg[a_m^{(p)}(\omega) + \sum_{q \neq p} \sum_n b_n^{(q)}(\omega) H_{m-n}(n_0 k R_{q,p}) \times e^{i(n-m)\theta_{q,p}} \Bigg] e^{im\phi_p} J_m(n_0 k |\mathbf{r} - \mathbf{r}_p|). \tag{3}$$

Here, F denotes the z component of the electric field (corresponding to TM polarization) or the magnetic field (corresponding to TE polarization), m is the azimuthal mode number, n_0 is the refractive index of surrounding media (air), and k is the vacuum wave number. The refractive index of the disks n_{d} (assumed to be equal for all disks) was obtained as the effective mode index of a slab waveguide with the thickness of the disks. The expansion coefficients $b_m^{(p)}$, $d_m^{(p)}$, and $a_m^{(p)}$ define contributions of the mth mode of the pth disk to the respective fields. The polar angle ϕ_p is defined in the local coordinate system of the pth disk centered at $\mathbf{r}_p$. The incident field (3) on the pth disk has contributions from the scattered field of all other disks $q \neq p$, with $R_{q,p}$ and $\Theta_{q,p}$ as the radial and polar coordinates, respectively, of the pth disk in the local coordinate system of the qth disk. Using boundary conditions as described in Ref. [18], the expansion coefficients of the scattered and internal field can be related to the expansion coefficients of the incoming field. From this, the total field can be calculated with Eqs. (1)–(3) for a certain spatial and spectral range.

As stated in Ref. [18], the spectrum of the coupled disks is well described by a resonant mode approximation taking into account only one fundamental WGM mode (with the largest possible azimuthal mode number at a certain resonance wavelength) and neglecting the coupling to higher-order modes (smaller mode numbers m). The calculation of the field distribution in the resonant approximation leads to discontinuities of the field at the disk boundary also for physically continuous fields (like the z component of the magnetic field for TE polarization). Therefore, for the exact field calculation, one has to take into account all possible modes with azimuthal mode numbers $m = -m_{\max}, \ldots, m_{\max}$, with $m_{\max}$ chosen so that convergence of the field distribution is guaranteed (usually it depends on the symmetry of the incident field).

When dealing with the coupling of all mode numbers m, the incident field also has to be reconsidered. In order to match the experimental conditions of a tapered fiber excitation in a simplest approximation, a plane wave with a one-dimensional Gaussian distribution perpendicular to the propagation direction was used. With the center of the Gaussian distribution $\mathbf{r}_0 = (x_0, y_0)$ and the width w corresponding to the width of the tapered fiber mode (with effective mode index n_{eff}), the global exciting field can be written as

$$F_{\text{inc,glob}} = A e^{i n_{\text{eff}} k [(x-x_0)\cos\delta - (y-y_0)\sin\delta]} \times e^{-[(x-x_0)\sin\delta + (y-y_0)\cos\delta]^2/w^2}. \tag{4}$$

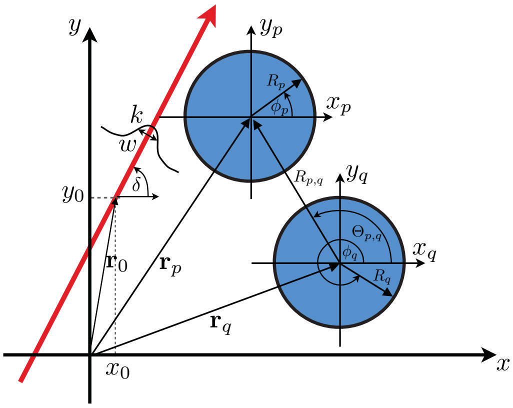

FIG. 2. (Color online) Sketch of used quantities and coordinate relations. The red arrow marks the direction of the Gaussian distribution of the incident field through the tapered fiber.

Without loss of generality, the amplitude A is set to 1, and δ is the angle between the tapered fiber axis and the x axis of the global coordinate system (see Fig. 2 for geometrical relations). In order to use Eqs. (1)–(3), the expansion coefficients $a_m^{(p)}$ in Eq. (3) can be calculated from the overlap integral of the local incident field (Bessel function expansion in the coordinate system centered at the pth disk) with the global Gaussian incident field at the boundary of each disk,

$$a_m^{(p)} = \frac{1}{2\pi |J_m(n_0 k R^{(p)})|^2} \int_0^{2\pi} d\phi \big[J_m^*(n_0 k R^{(p)}) e^{-im\phi} \times e^{i n_{\text{eff}} k [(x_{\text{gl}}^{(p)} - x_0)\cos\delta - (y_{\text{gl}}^{(p)} - y_0)\sin\delta]} \times, e^{-[(x_{\text{gl}}^{(p)} - x_0)\sin\delta + (y_{\text{gl}}^{(p)} - y_0)\cos\delta]^2/w^2} \big]. \tag{5}$$

Here, $R^{(p)}$ is the radius of the pth disk and ϕ is the angle in the local coordinate system of the pth disk, whereas $(x_{\text{gl}}^{(p)}, y_{\text{gl}}^{(p)})$ are the coordinates of all points of the boundary of the pth disk in the global coordinate system.

As an example, the calculated spectrum and intensity distribution of a fundamental mode ($m = 35$, $\lambda \approx 1.579\ \mu$m) of three coupled disks is shown in Fig. 3. The disks have a radius of 7.5 μm, a thickness of 1 μm, and a material refractive index of 1.445. Using the resonant mode approximation (assuming that initially the mode is already excited in one disk) leads to a fully symmetric spectrum [Fig. 3(a)] showing four peaks in the expansion coefficients of the scattered field. Due to excitation of the first disk, the spectrum of this coefficient is different from those of disks 2 and 3, which are equal due to symmetry reasons. Figure 3(b) shows the same coefficients when the full model is used. In this case, disk 1 is excited by the Gaussian distribution, as shown in Fig. 3(e), and the mode numbers range from $m = -45$ to $m = 45$, which is enough to properly approximate the asymmetric incident field at the rim of each disk by Eq. (5). Due to the coupling to higher-order modes, the resonances get slightly red shifted and broadened. Nevertheless, the resonance peaks can be identified [marked by the dotted lines between Figs. 3(a) and 3(b)]. The degeneracy between the expansion coefficients of disks 2 and 3 is lifted due to the asymmetry of the exciting field. In order to test the reliability of the model, a rigorous three-dimensional finite difference time domain (FDTD) simulation of the structure was performed. Here the excitation through the tapered fiber was taken into account rigorously. To suppress the influence of back reflections of outgoing waves, the calculation domain was enclosed by perfectly matched layers. The spectrum [the interesting part is shown in Fig. 3(c)] was calculated from time series of the electric field recorded by monitors placed in

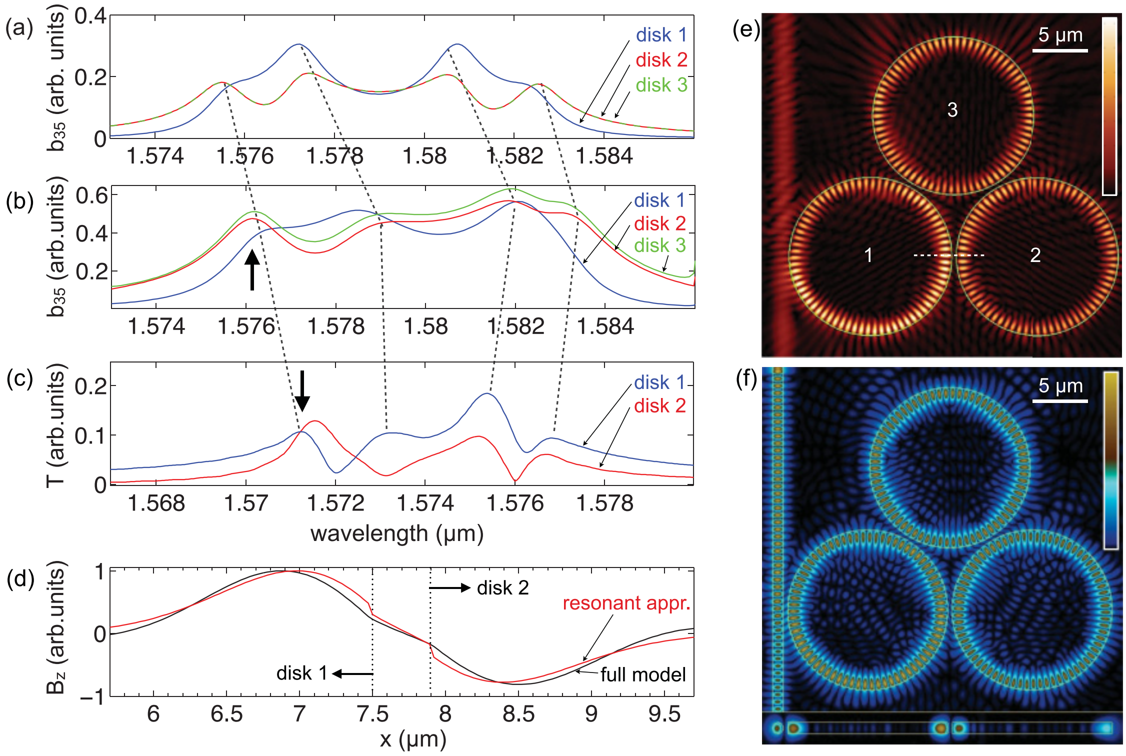

FIG. 3. (Color online) Calculation of the spectrum and intensity distribution of three coupled disks of equal size (radius 7.5 μm, thickness 1 μm, refractive index 1.445, all gaps 400 nm). The splitting of the fundamental mode ($m = 35$) is observable for (a) the resonant approximation and (b) the full model taking into account coupling to higher-order modes. Here the expansion coefficient $b_{m=35}$ for the field in each disk (disk 1, blue; disk 2, red; disk 3, green) is plotted. The intensity distribution of the mode marked by an arrow in (b) is shown in (e) using the full model. A comparison to a rigorous three-dimensional FDTD simulation (spatial resolution 30 nm) shows good agreement for (c) the spectrum, as well as for (f) the intensity distribution [same mode marked by the arrow (c)]. Only two field monitors in disks 1 and 2 were used for the spectrum calculation, so the green line for disk 3 is missing in (c). A comparison of the magnetic field (which needs to be continuous across boundaries) along the dashed line in (e) for the resonant approximation and the full modal expansion in (d) underlines the need for the full model in order to calculate the fields correctly.

disks 1 and 2 for the case of a pulsed excitation. Even though the spectrum is blue shifted and the splitting is slightly less than that of the mode expansion method, it also shows four peaks. For the first resonance peak [marked by an arrow in Figs. 3(b) and 3(c)], the intensity distribution was calculated with both methods and is shown in Fig. 3(e) for the modal expansion and in Fig. 3(f) for the FDTD (snapshot of a continuous-wave excitation), which shows very nice agreement.

To point out the importance of using the full modal expansion for the correct calculation of the fields, a comparison of the normalized magnetic field across the boundaries between disks 1 and 2 [marked by the dashed line in Fig. 3(e)] is shown in Fig. 3(d). The used resonant approximation leads to unphysical discontinuities, as mentioned above, whereas the field calculated with the full model shows a smooth transition across the boundaries.

It is worth noting that the method described above is a good compromise between reasonable fields of (also large) coupled disk ensembles and a relatively fast and flexible calculation. The approximation of the excitation by a Gaussian distribution does not take into account any influences of the exciting tapered fiber, but the incident-field distribution is well described. Therefore, it is also not possible to extract any transmission and reflection signals comparable to the experimental situation. This would be possible if the tapered fiber would be considered as a waveguide (with boundaries) in the calculation domain, which leads to an additional expansion of the waveguide field and boundary conditions (overlap integrals) and would make the calculation much more complex (for comparison, a more rigorous model for smaller ring resonators is presented in Ref. [25]).

B. Coupled-mode theory including the scattering SNOM tip

In order to describe the experimental situation more properly, the coupled-mode theory [22,26] was used to model the transmission and reflection spectra by including the tapered fiber coupling for excitation as well as the SNOM tip as a perturbation of the system. Using this approach, it is also straightforward to take into account scattering losses due to surface roughness present in the disk samples under investigation. As a consequence of the surface roughness, the clockwise (cw) and counterclockwise (ccw) propagating modes in one disk are coupled. Using the notation of Sec. III A, this means that even in a single disk, modes with opposite sign of the azimuthal mode number m couple to each other. Taking into account only a single cw and ccw mode in each disk (for the spectrum, the single mode approximation is valid for the samples under investigation), the dynamics of the mode amplitudes of N coupled disks can be written as [6]

$$\dot{d}_{\mathrm{cw}}^{(p)} = [i\omega_0 - \Gamma_0 - \Gamma_{\mathrm{ext}}]d_{\mathrm{cw}}^{(p)} + i\Gamma_{\mathrm{c}}d_{\mathrm{ccw}}^{(p)} + i\sum_{q=1,q\neq p}^{N}\Gamma_{pq}d_{\mathrm{ccw}}^{(q)} + i\sqrt{2\Gamma_{\mathrm{ext}}^{(p)}}a_{\mathrm{cw}}^{\mathrm{in}}, \tag{6}$$

$$\dot{d}_{\mathrm{ccw}}^{(p)} = [i\omega_0 - \Gamma_0 - \Gamma_{\mathrm{ext}}]d_{\mathrm{ccw}}^{(p)} + i\Gamma_{\mathrm{c}}d_{\mathrm{cw}}^{(p)} + i\sum_{q=1,q\neq p}^{N}\Gamma_{pq}d_{\mathrm{cw}}^{(q)} + i\sqrt{2\Gamma_{\mathrm{ext}}^{(p)}}a_{\mathrm{ccw}}^{\mathrm{in}}. \tag{7}$$

Here, $\Gamma_0 = \omega_0/(2Q_0)$ are the intrinsic material and radiation losses related to the intrinsic quality factor Q_0, and $\Gamma_{\mathrm{ext}} = \omega_0/(2Q_{\mathrm{ext}})$ denotes the external coupling losses introduced by the tapered optical fiber related to an external quality factor Q_{ext}. The above-mentioned coupling between the cw and ccw mode in a single disk due to surface roughness is described by the coupling rate Γ_{c} and the coupling between neighboring disks is accounted for with the coupling rate Γ_{pq}. The pump through the tapered fiber is described by $a_{\mathrm{cw,ccw}}^{\mathrm{in}}$. It is worth noting that d and a were used to be consistent to the notation in Sec. III A, but one has to keep in mind that especially the external pumping $a_{\mathrm{cw,ccw}}^{\mathrm{in}}$ is not comparable to the modal expansion coefficients $a_{\mathrm{m}}^{(p)}$ of the incident field in Eq. (3). The relation between these quantities is expressed by the external coupling rate Γ_{ext} from the overlap of the tapered fiber mode with a certain disk mode, which can be handled only numerically.

The scattering by the SNOM tip can be described in a semiquantum optical framework [23]. When the tip is located within the optical near field of the disk mode, the photons can be scattered into the same or the counterpropagating disk mode, or into a reservoir mode (additional scattering loss). Modeling the SNOM tip as a single subwavelength (Rayleigh) scatterer, its interaction with the microresonator can be described using dipole approximation [27]. The electric field of the resonator mode induces a dipole moment $\mathbf{p} = \epsilon_0\alpha\mathbf{E}_{\mathrm{mode}}$ in the scatterer, which can be approximated as a spherical particle with radius R_{tip} and electric permittivity ϵ_s, surrounded by a medium of electric permittivity ϵ_m having a polarizability of

$$\alpha = 4\pi R_{\mathrm{tip}}^3\frac{\epsilon_s - \epsilon_m}{\epsilon_s + 2\epsilon_m}. \tag{8}$$

Following the derivation in the supplementary information of [23], the coupling coefficients (g, coupling to disk mode; g', coupling to reservoir mode) can be expressed as

$$g = -\frac{\alpha f^2(\mathbf{r}_{\mathrm{tip}})\omega_0}{2V_{\mathrm{mode}}}, \tag{9}$$

$$g' = -\frac{\alpha f^2(\mathbf{r}_{\mathrm{tip}})\omega_0}{2\sqrt{V_{\mathrm{mode}}V_j}}(\hat{\mathbf{n}}_{\mathrm{mode}}\cdot\hat{\mathbf{n}}_j), \tag{10}$$

where $V_{\mathrm{mode},j}$ denotes the quantization (or mode) volumes of the cavity (reservoir) mode, $\hat{\mathbf{n}}_{\mathrm{mode},j}$ are the respective field unit vectors, and $f(\mathbf{r}_{\mathrm{tip}})$ accounts for the SNOM tip position $\mathbf{r}_{\mathrm{tip}}$ in the field distribution of the mode f. While the induced Rayleigh scattering to a disk mode leads to an additional splitting of the observed resonances, the coupling to reservoir modes act as an additional loss channel and can be described by a damping rate γ_{rs}, which can be derived using a Weisskopf-Wigner approximation,

$$\gamma_{\mathrm{rs}} = \frac{\alpha^2 f^2(\mathbf{r}_{\mathrm{tip}})\omega_0^4}{6\pi c^3 V_{\mathrm{mode}}}. \tag{11}$$

This will lead to a broadening of the observed resonances. With g from Eq. (9), $\Gamma_{\mathrm{rs}} = \gamma_{\mathrm{rs}}/2$, and by introducing slowly varying mode amplitudes $d_{\mathrm{cw,ccw}} = \bar{d}_{\mathrm{cw,ccw}}e^{i\omega t}$ (the bar is omitted in the following), Eqs. (6) and (7) can be written as

$$\dot{d}_{\mathrm{cw}}^{(p)} = [i(-\Delta\omega + g) - \Gamma]d_{\mathrm{cw}}^{(p)} + [i(\Gamma_{\mathrm{c}} + g) - \Gamma_{\mathrm{rs}}]d_{\mathrm{ccw}}^{(p)} + i\sum_{q=1,q\neq p}^{N}\Gamma_{pq}d_{\mathrm{ccw}}^{(q)} + i\sqrt{2\Gamma_{\mathrm{ext}}^{(p)}}a_{\mathrm{cw}}^{\mathrm{in}}, \tag{12}$$

$$\dot{d}_{\mathrm{ccw}}^{(p)} = [i(-\Delta\omega + g) - \Gamma]d_{\mathrm{ccw}}^{(p)} + [i(\Gamma_{\mathrm{c}} + g) - \Gamma_{\mathrm{rs}}]d_{\mathrm{cw}}^{(p)} + i\sum_{q=1,q\neq p}^{N}\Gamma_{pq}d_{\mathrm{cw}}^{(q)} + i\sqrt{2\Gamma_{\mathrm{ext}}^{(p)}}a_{\mathrm{ccw}}^{\mathrm{in}}, \tag{13}$$

with $\Gamma = \Gamma_{\mathrm{rs}} + \Gamma_0 + \Gamma_{\mathrm{ext}}$ and $\Delta\omega = \omega - \omega_0$. Here it is assumed that the SNOM tip couples only the modes in one disk, also when it is positioned in the gap region between two disks, where in reality it can couple the modes of both disks. In the context of microdisk mode mapping, one is interested in the steady-state solutions $\dot{d}_{\mathrm{cw,ccw}} = 0$. This leads to a system of coupled linear equations, which can be compactly written in matrix form

$$\mathbf{M}\cdot\mathbf{d} = \mathbf{a}, \tag{14}$$

with the vector of $2N$ unknown mode amplitudes

$$\mathbf{d} = \left(d_{\mathrm{cw}}^{(1)}, d_{\mathrm{ccw}}^{(1)}, \ldots\right)^T, \tag{15}$$

and known input amplitudes

$$\mathbf{a} = \left(\ldots, -i\sqrt{2\Gamma_{\mathrm{ext}}^{(p)}}a_{\mathrm{cw}}^{\mathrm{in}}, i\sqrt{2\Gamma_{\mathrm{ext}}^{(p)}}a_{\mathrm{ccw}}^{\mathrm{in}}, \ldots\right)^T. \tag{16}$$

With respect to the experimental situation, it is assumed that only one disk (p) of the coupled ensemble is excited by the tapered fiber and the pump is single directional ($a_{\mathrm{ccw}}^{\mathrm{in}} = 0$). The mode amplitudes $\mathbf{d}$ can then be found by matrix inversion, and the transmission ($\mathcal{T}$) and reflection ($\mathcal{R}$) through the taper can be described by

$$\mathcal{T} = \left|1 + \frac{i\sqrt{2\Gamma_{\mathrm{ext}}^{(p)}}d_{\mathrm{cw}}^{(\mathrm{p})}}{a_{\mathrm{cw}}^{\mathrm{in}}}\right|^2, \tag{17}$$

$$\mathcal{R} = \left|\frac{i\sqrt{2\Gamma_{\mathrm{ext}}^{(p)}}d_{\mathrm{ccw}}^{(\mathrm{p})}}{a_{\mathrm{cw}}^{\mathrm{in}}}\right|^2. \tag{18}$$

Using the model in Sec. III A to calculate the two-dimensional intensity distribution of the excited mode, Eqs. (9) and (10) give corresponding distributions of the tip-induced scattering strength, which results in theoretical transmission and reflection mode maps [Eqs. (17) and (18)]. All unknown coefficients in Eqs. (12) and (13) can be obtained by independent measurements without SNOM tip perturbation.

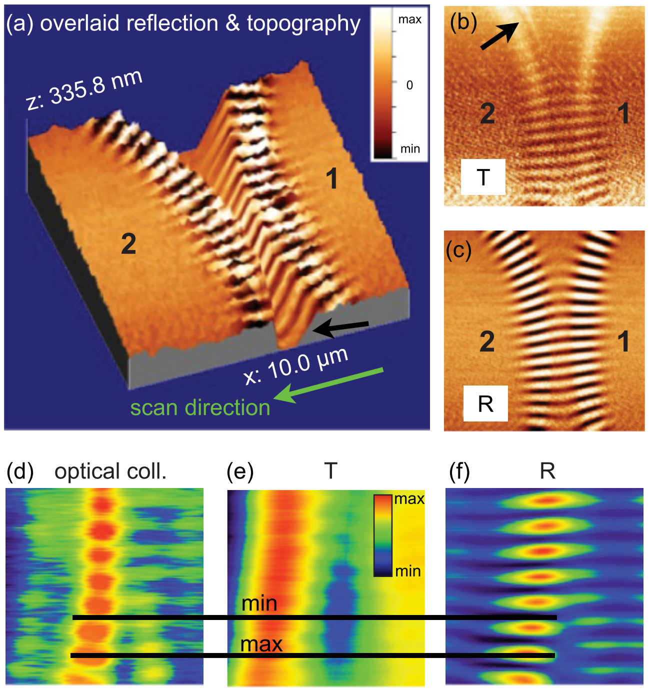

FIG. 4. (Color online) Typical measurement signals for scanning across the gap of two coupled disks: (a) overlaid reflection and topography images, (b) only transmission signal, and (c) only reflection signal measured by scattering SNOM. A comparison with an aperture SNOM measurement in collection mode shows the relation between (d) the real mode structure and the measured (e) transmission and (f) reflection signals.

IV. EXPERIMENTAL CHARACTERIZATION

The interaction of the scattering SNOM tip with the excited disk leads to several features in the experimental data, which are discussed in the following. A typical reflection measurement signal (here scanning across the gap of two coupled disks) overlaid on the obtained topography of the sample is shown in Fig. 4(a) [transmission and reflection, respectively, in Figs. 4(b) and 4(c)]. Generally, the contrast obtained in the reflection signal is better than for the transmission signal. The reflection signal remains unperturbed when the tip is positioned outside the mode volume or over the substrate, whereas it increases and decreases when the tip is above the location of the mode. In particular, the decrease of the reflection signal is surprising because the method is sensitive to the mode intensity only. When the tip is placed in a node of the mode distribution, it should not have any influences on the measured transmission and reflection signals. In order to exclude systematic measurement errors, we compared the method with the direct collection of the optical near-field distribution by an aperture SNOM tip. Although the aperture tip is larger compared to the apertureless scattering SNOM tip, it can also be used to measure transmission [Fig. 4(e)] and reflection [Fig. 4(f)] mode maps in addition to the direct collection signal [Fig. 4(d)]. As expected, the optical collection signal is always larger than the background also when the tip is placed in a node of the disk mode. Due to the large tip size, the transmission signal gets blurred out and the mode structure in the azimuthal direction can hardly be resolved, whereas the reflection signal is almost the same as for the scattering SNOM tip showing values smaller and larger than the background. From the comparison of the collection and reflection signals, one can see that the tip in an antinode (node) of the disk mode results in a stronger (weaker) signal compared to the unperturbed reflection.

Another feature visible in the measured mode maps is a narrow stripe of unperturbed signal level in the top left region of Fig. 4(b) marked by the arrow [also visible in Fig. 4(c)]. This can be explained by the movement of the SNOM tip across the sample. Usually, the starting point is chosen above a disk (here disk 1) and the fast scan axis is almost normal to the rim of the disk (or gap between two disks). In Fig. 4(a), the scan direction is highlighted and from the cross section of the topographical data (black arrow) one can see that the tip drops smoothly down toward to the substrate when it (the very end of the tip) senses the rim of the disk. Due to the sample structure, the tip reaches its minimum z position during the scan. When the tip (not the very end of it) recognizes the other disk, it retracts much faster (indicated by the steeper transition) and the tip touches the sidewall of the disk. This leads to a very strong interaction and a strong signal. Due to the fast retraction, the tip overshoots when reaching the top surface level of the disk, leading to a weaker interaction and signal. The effect is more pronounced when the separation between the disks becomes larger but has no significant influence on the measured data in the region where the disks are closest to each other.

A. Single disk mode mappings

In order to test the theoretical model and its ability to describe the experimental data, the simplest case of a single excited disk was considered. With this restriction, the steady-state solutions of the cw and ccw mode amplitudes [Eqs. (12) and (13)] can be given explicitly by

$$d_{\mathrm{cw}} = -i\sqrt{2\Gamma_{\mathrm{ext}}}a_{\mathrm{cw}}^{\mathrm{in}}[i(-\Delta\omega + g) - \Gamma]/D, \qquad (19)$$

$$d_{\mathrm{ccw}} = i\sqrt{2\Gamma_{\mathrm{ext}}}a_{\mathrm{cw}}^{\mathrm{in}}[i(\Gamma_{\mathrm{c}} + g) - \Gamma_{\mathrm{rs}}]/D, \qquad (20)$$

with the denominator

$$D = [i(-\Delta\omega + g) - \Gamma]^2 - [i(\Gamma_{\mathrm{c}} + g) - \Gamma_{\mathrm{rs}}]^2. \qquad (21)$$

The unknown parameters Γ_0, Γ_{c}, and ω_0 can be obtained from an independent spectrum measurement of the weak excited disk, as shown in Ref. [6], when the tip is absent and using the theoretical model without SNOM tip perturbation for fitting. For the measured disk, the obtained values are given in Table I.

For the perturbed system, the unknown parameters g, Γ_{rs}, and Γ_{ext} can be narrowed down to certain ranges. The coupling coefficient g and the scattering rate Γ_{rs} depend on the polarizability of the SNOM tip, the mode volume, and the intensity distribution of the mode. The mode volume and the normalized field strength at the position of the tip above the disk can be found from finite element simulations (for values, see Table I), whereas the intensity distribution can be calculated using the model in Sec. III A. The polarizability [Eq. (8)] depends on the radius of the tip (approximated as a sphere) and its electric permittivity. Starting from the approximated value for the polarizability, it is used as a fit

TABLE I. Model parameters.

Parameter	Value	Source
$\lambda_0 = 2\pi c/\omega_0$	1556.055 nm	Fit
Γ_0	1.55 GHz	Fit
Γ_c	2.89 GHz	Fit
R_{tip}	50 nm	SEM meas.
ϵ_m	$-131.718 + i12.639$	Ref. [28]
V_{mode}	6.7×10^{-17} m^3	FEM sim.

parameter because the simple spherical shape approximation may not be accurate for the used SNOM tips. The other parameter used for adjustment of the calculation to the measured data is the external coupling rate Γ_{ext}. Although it is set at the beginning of the mapping, fluctuations of the tapered fiber position during the measurement can change the value.

For the test of the model, a TM polarized fundamental disk mode with a resonance at 1556.055 nm was chosen. The transmission signal is shown in Fig. 5(a), where the taper is slightly overcoupled (no splitting is observable). The laser wavelength was scanned stepwise through the resonance and, at each wavelength (marked by a red line), a mode map was recorded. As already mentioned, the coupling condition possibly changes slightly for each of the measurements. The mode maps were taken close to the rim of the disk but with the tip not scanning across to avoid vertical tip movements and the above-mentioned artifacts. The scan window has a size of 1.5×1.5 μm^2 and the 11 transmission and reflection mode maps were arranged successively in Figs. 5(c) and 5(e). The intensity distributions for the respective wavelengths were calculated for the same section of the disk and arranged in the same way [Fig. 5(b)]. With this data, the coupled-mode model was used to calculate the corresponding transmission [Fig. 5(d)] and reflection [Fig. 5(f)] mode maps. The first, most obvious characteristic, seen when comparing simulation and measurement, is the expected phase shift that the mode undergoes if one scans through the resonance. The shift is seen in all of the picture series in Figs. 5(b)–5(f) and tracked by the dotted lines. For the experimental data shown in Figs. 5(c) and 5(e), the transmission again shows less contrast

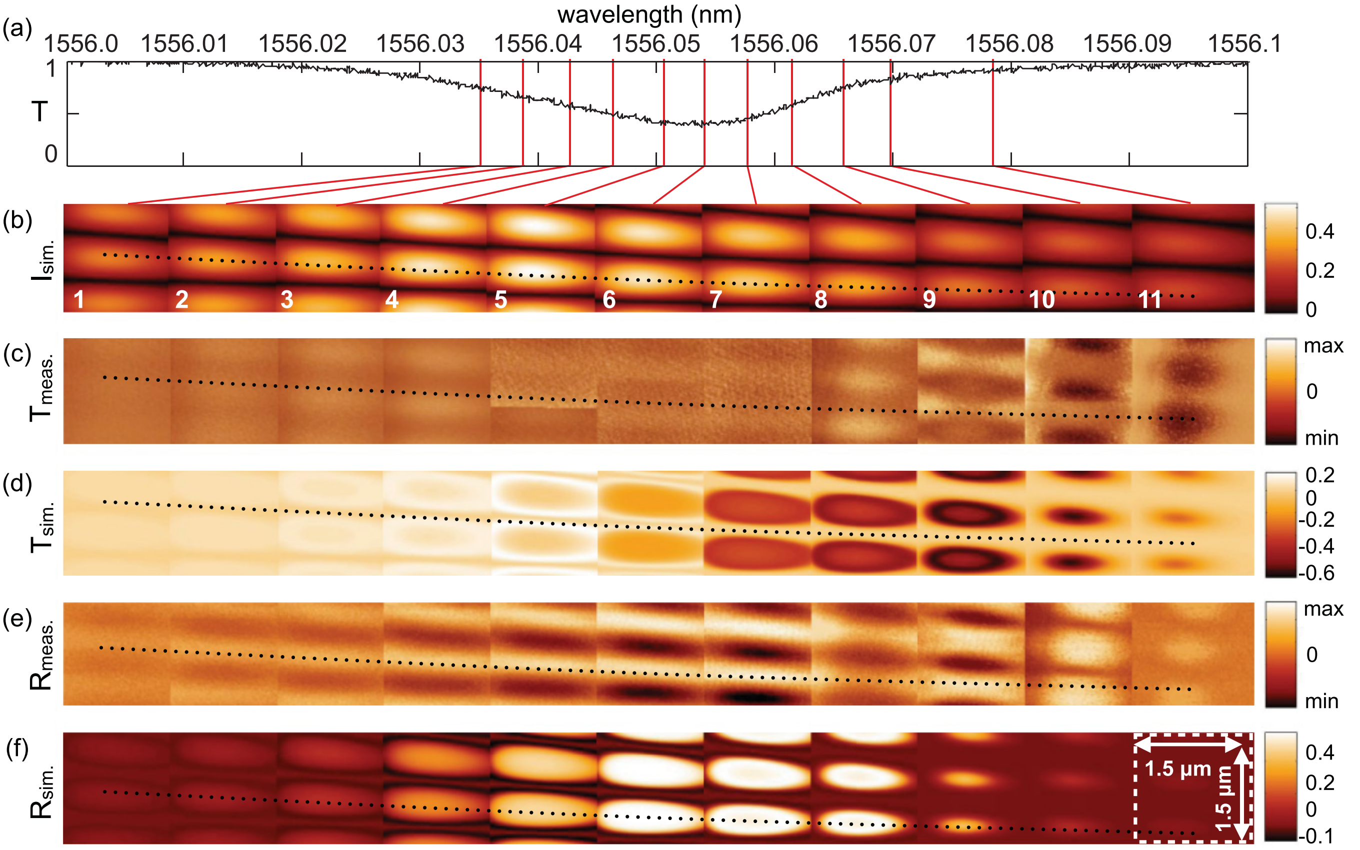

FIG. 5. (Color online) Successive mode mappings for a stepped wavelength scan through a resonance of a single disk using the perturbation of a scattering SNOM tip. For each of the 11 wavelengths marked in the transmission spectrum, (a) a scan window of 1.5×1.5 μm^2 [which is highlighted in (f), frame 11] was mapped and arranged horizontally to a picture series (numbered 1 to 11) for (c) transmission and (e) reflection signals. For the same area of the disk (and arranged in the same way), the intensity distributions of the mode were calculated in (b), and from this the theoretical (d) transmission and (f) reflection signal maps were obtained. The dotted lines in (b)–(f) indicate the phase shift that the mode distribution shows when scanning through the resonance. A good agreement is obtained for the shift of the signal maximum in transmission [(e), (f), frames 6, 7] and reflection [(c), (d), frames 8, 9] compared to the expected intensity maximum of the mode [(b), frame 5]. Also, complex patterned maps are obtained from the calculations in agreement with the measured signals [ring structure in (c), (d), frame 9].

than the reflection. Unlike the intensity, which shows only positive values, the calculated transmission and reflection maps show both positive and negative values, which is in agreement with the measured data. As another detail, one can see that the calculated intensity maximum [Fig. 5(b), frame 5] corresponding to the minimum in the transmission spectrum [Fig. 5(a)] does not coincide with the strongest signal either in reflection or transmission. Also, the maximum signal in the transmission maps [Fig. 5(c), frames 9, 10] does not coincide with the maximum signal in the reflection maps [Fig. 5(e), frames 6, 7], which is well reproduced by the calculated maps. From the comparison with the optical measurements (see Fig. 4), it is expected that the intensity maxima and maxima in the reflection maps coincide, which is also seen here [compare Figs. 5(b), 5(d), and 5(f)]. Additionally, one can see that this is also the case for the transmission maps for the lower wavelengths. For the longer wavelengths, a phase shift occurs [Fig. 5(c), frames 10, 11], which is not observed in the calculations. This could have happened due to a stronger change in the excitation condition to a regime where transmission and reflection maps are inverted. This regime was also observed for mappings in two coupled disks in an independent measurement (not shown here). The most surprising detail, however, is the ringlike structure in the transmission maps observable in both measurement and calculation [Figs. 5(c) and 5(d), frame 9]. At this particular wavelength, under the present coupling condition and scattering rate due to the tip, the increasing intensity (when the tip moves into an antinode) causes a decrease in the transmission (color changes to black), whereas at the maximum intensity (center of the antinode) the transmission again increases. The simulation of this special feature together with the above-mentioned details show that the described model is capable of explaining the measured results by the rather simple dipole approximation of the interaction of the SNOM tip with the disk resonator mode. From this, we conclude that the measured transmission and reflection signals are related to the actual intensity distributions of the WGMs in coupled microdisks.

V. EIGENMODE MAPPING OF COUPLED MICRODISKS

In the following, eigenmode mappings of two and three coupled microdisks in different arrangements are presented. Depending on the number of coupled disks and the symmetry of their arrangement, a splitting into a certain number of normal modes occurs. In the presented analysis, only fundamental modes with a single ring of intensity maxima along the rim of the disks were investigated. In this case, the mapping of the mode distribution of the whole sample is not necessary because from theoretical calculations it is expected that the differences of the intensity distributions of the modes emerge in the gap regions. Hence, the mappings were taken across the gap of neighboring disks only. For each gap, a squared scan window of $5 \times 5\ \mu\text{m}^2$ or $10 \times 10\ \mu\text{m}^2$ was chosen. The advantages of this approach are the decrease of scanning time, especially for large arrangements, and the avoidance of measurement artifacts when scanning far from the gap regions, as mentioned in Sec. IV.

For the comparison with calculations, the modal expansion method (Sec. III A) was used. On the one hand, this is motivated by the fact that for all measured modes and gaps, the coupling conditions during the scan could be different, which results in a large number of simulations (parameter adjustments) needed. On the other hand, the calculated intensity distribution from the rigorous modal expansion agrees quite nicely with the measured reflection mode maps for a relatively large range of detunings from the exact resonance wavelength. This leads to fast and reliable calculations for comparison with experimental data.

A. Two coupled microdisks

For the coupling of two microdisks, a splitting in two modes is expected and observed in the measured spectra [18]. This can be understood by the symmetric and antisymmetric combination of the eigenmodes of each of the single disks. The difference in the intensity distribution of both modes can be observed when scanning across the gap region. In Fig. 6, the respective mode mappings and calculated intensity distributions are shown. For the antisymmetric mode [short wavelength resonance in Fig. 6(a)], the fields in both disks have a phase difference of π, which leads to a destructive interference of the fields in the gap region. Therefore, the recorded reflection mode map in Fig. 6(c) shows no signal exactly in the gap between the disks, which is in excellent agreement with the calculated intensity for the same section of the sample marked in Fig. 6(b). The long wavelength resonance is the symmetric mode, for which the fields in both disks are

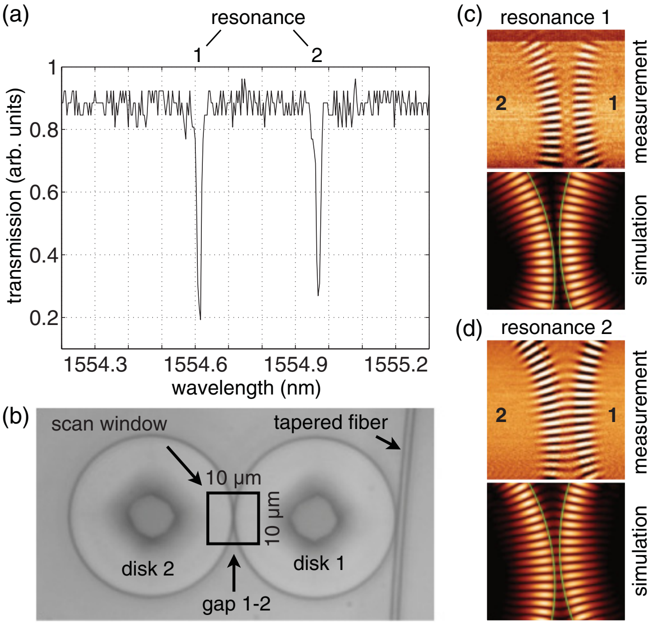

FIG. 6. (Color online) (a) The measured transmission for two coupled disks shows splitting in two eigenmodes: antisymmetric (resonance 1) and symmetric (resonance 2) mode. (b) In the top view of the measured sample with the tapered fiber for excitation of disk 1, the scan region of $10 \times 10\ \mu\text{m}^2$ across the gap is highlighted. The measured reflection mode maps and calculated mode intensity distributions are compared for the (c) antisymmetric and (b) symmetric mode. In each measurement square in (c) and (d), the numbers highlight the particular disk, whereas in the corresponding simulation, the green lines mark the disk's rim.

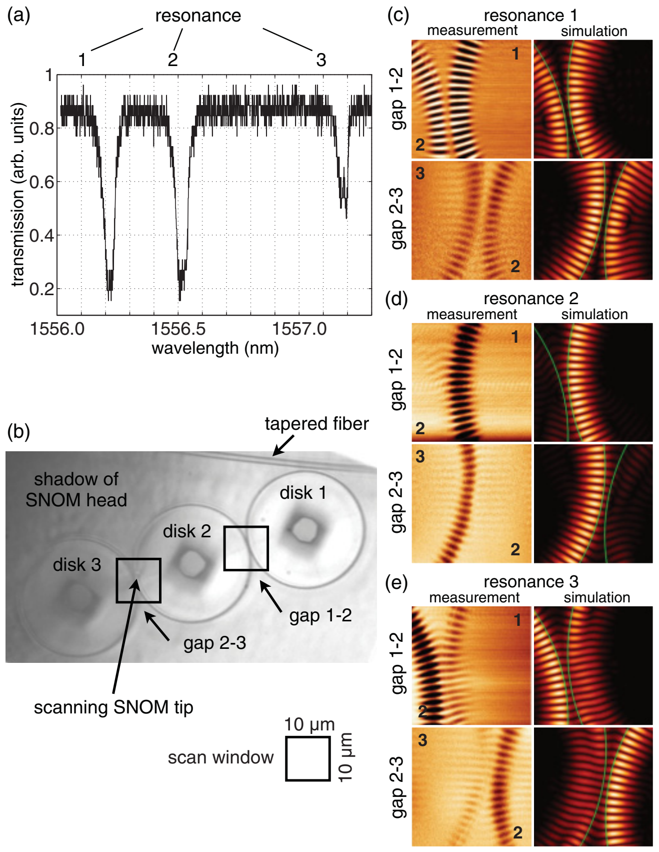

FIG. 7. (Color online) (a) The measured transmission for three coupled disks in a linear arrangement shows splitting in three eigenmodes. (b) In the top view of the measured sample, the scan windows are highlighted. On the left of the picture the shadow of the SNOM head is seen while scanning the gap between disks 2 and 3. The measured reflection mode maps and simulated mode intensity distributions are compared for both gaps and all resonance dips in (a), starting from the (c) antisymmetric mode or resonance 1, over the (d) middle resonance 2, to the (e) symmetric mode or resonance 3. In each measurement square in (c)–(e), the numbers highlight the particular disk, whereas in the corresponding simulation, the green lines mark the disk's rim.

in phase. This leads to constructive interference in the gap region, which can be seen by the strong signal in the reflection mode map in Fig. 6(d). Again, this is in agreement with the calculated intensity distribution.

B. Three coupled microdisks in linear arrangement

For the case of three coupled disks in a line arrangement, a splitting in three normal modes is expected. The measured spectrum in Fig. 7 shows the three modes for which the mode mappings were recorded. As mentioned in Ref. [18] for three identical disks coupled in a line, the splitting of the modes should be symmetric. The observed smaller spectral distance of the middle resonance to the short wavelength resonance than to the longer wavelength resonance indicates a size mismatch between the two outer disks and the inner disk. Fitting of the spectrum using the rigorous modal expansion shows that the asymmetry can be explained by a radius of the middle disk to be 3 nm larger than that of the other disks, which is in the range of the fabrication accuracy. In Fig. 7(b), the scan regions across the gaps between the disks are highlighted. On the left side, the image is blurred a little, which is due to the SNOM head scanning the gap between disks 2 and 3 and shadowing the sample. In Figs. 7(c)–7(e), the recorded reflection mode maps are shown and compared to the calculated intensity distributions at the three resonances in Fig. 7(a). Again the short wavelength resonance is the antisymmetric mode, where the fields in adjacent disks show a phase difference of π, which leads to destructive interference in the gaps between the disks. In the measured data, this can be seen clearly because no signal changes occur when the SNOM tip is exactly located over the gap. The differences in the signal strength and characteristics between the measured maps of gap 1-2 and gap 2-3 are due to the procedure itself. For one gap, all modes were mapped first before the SNOM head was moved to the other gap. This requires new alignment of the taper-disk gap as well as the resonance wavelength for each mode. In Sec. IV, it was shown that these parameters have a strong influence on the characteristics of the recorded mode maps and it is unlikely to match exactly the same conditions for the complex system. Nevertheless, there is a nice agreement between the measurements and the calculated mode maps. For the middle resonance, the phase differences between the fields in adjacent disks is $\pi/2$, which leads to a cancellation of the field in the complete middle disk. This can be observed in the measurements as well as in the calculations. The long wavelength resonance, which is the symmetric mode, shows again a signal from all three disks, whereas the signal from the middle disk is strongest. Due to the zero phase difference of the fields in adjacent disks, the constructive interference leads to an intensity signal in the gap, which can be seen clearly in the measurements and simulations. One interesting detail when looking at the maps in Fig. 7(e) is the agreement in the relative signal strength in the weaker excited disks (1 and 3) when comparing measurement and simulation. Directly at the smallest gap region, the intensity in these disks is weaker than further away from the gap (upwards and downward along the rim) and the signal extends more toward the center of the disk.

C. Three coupled microdisks in triangular arrangement

For three identical disks in a triangular arrangement, a splitting in four resonances is expected, as shown in Sec. III A. The measured spectrum for the sample under investigation [Fig. 8(b)] shows six resonances [Fig. 8(a)]. This can be explained by a small size mismatch of the disks of a few nm and the resulting lift of degeneracy of modes, which for identical coupled disks have the same resonance wavelength but different mode distributions. The best results for the simulation were obtained for the radii of all disks being slightly different ($R_1 = 15.1008$, $R_2 = 15.0958$, and $R_3 = 15.1012$ μm). The weak resonances (unnumbered) in the spectrum belong to a mode with a different polarization, which spectrally overlap and get excited by cross-polarization coupling. For each of the numbered resonances, a mode map across each gap between the disks was recorded and is shown together with the simulation in Figs. 8(c)–8(h). The first resonance [Fig. 8(c)] is the antisymmetric mode with the fields

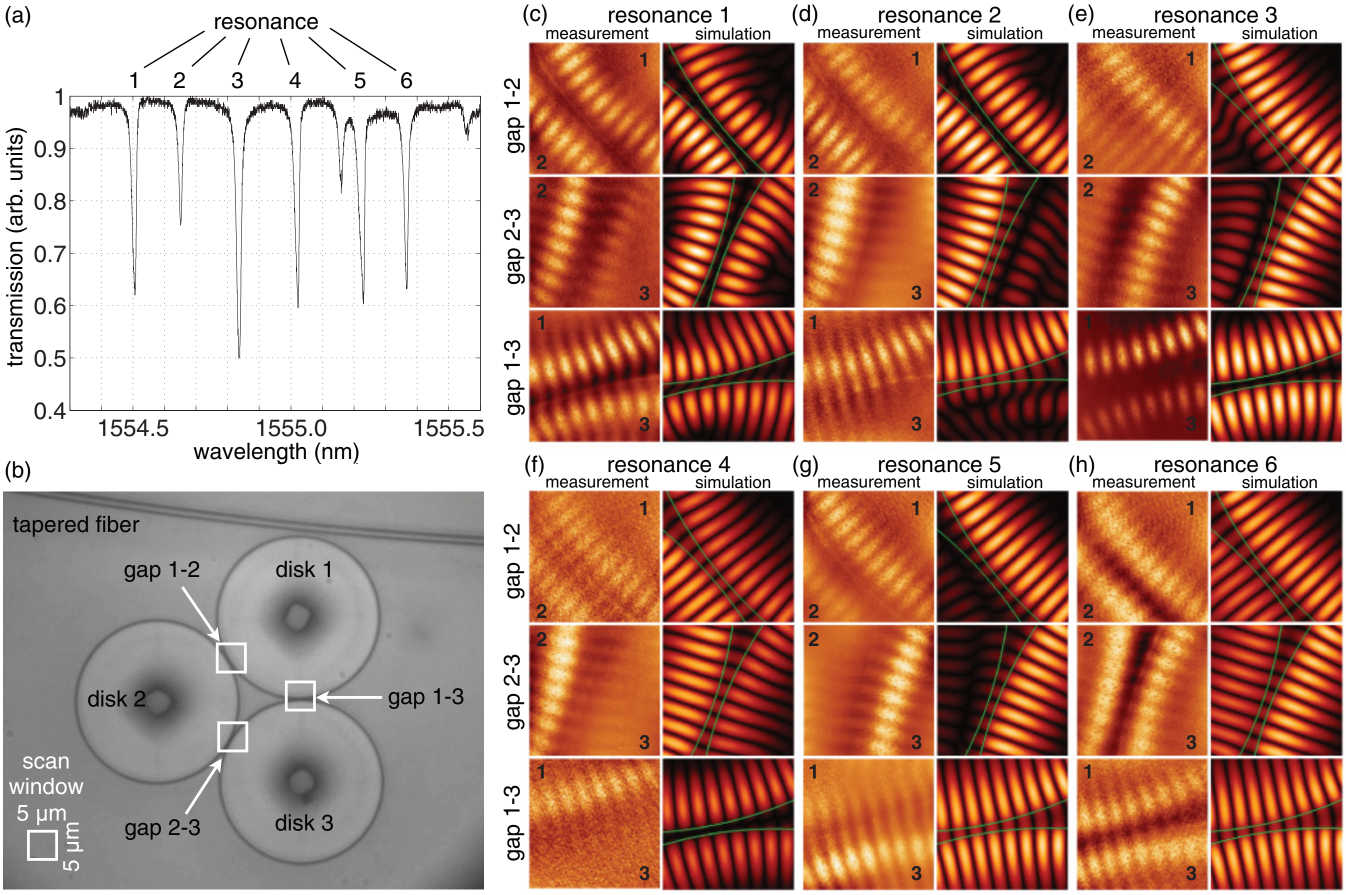

FIG. 8. (Color online) (a) Measured transmission spectrum for three coupled disks in a triangular arrangement shows splitting in six eigenmodes. The unnumbered dips belong to the other polarization state, which was not suppressed completely. (b) A top view of the measured sample with tapered fiber for excitation of disk 1. The white squares highlight the SNOM scan window (5×5 μm^2) with the resulting intensity distribution shown in (c)–(h) for each of the gaps (1-2, 2-3, 1-3) and the numbered resonances from (a). In each measurement square in (c)–(h), the numbers highlight the particular disk, whereas in the corresponding simulation, the green lines mark the disk's rim.

showing a phase difference of π in adjacent disks, which leads to cancellation of the field in the gaps. For the measurement of gap 1-3, the mode was not exactly excited at the same wavelength as for the other gaps, which can be seen by the slight phase difference between the fields in disks 1 and 3. Taking this into account in the simulation, the measured weak signal in the gap can be reproduced. The second mode in Fig. 8(d) shows no intensity in disk 3. The fields in disks 1 and 2 have a phase difference of π, whereas the difference of both disks to disk 3 is $\pi/2$, leading to a cancellation of the field in disk 3. For the third mode [Fig. 8(e)], no intensity from disk 2 could be measured. Now the fields on disk 1 and 3 have a π phase difference and each shows a difference of $\pi/2$ to disk 2. In the case of identical disks, the two cases [Figs. 8(d) and 8(e)] would be indistinguishable and the resonances in the spectrum would be degenerated, whereas the small radius difference leads to different energy levels, and hence distinguishable resonance wavelengths in Fig. 8(a). The calculated mode maps for both of the resonances are in good agreement with the measured maps. The mode maps for the resonances 4, 5, and 6 show the same characteristics but for the symmetric modes of the system. For resonance 4 shown in Fig. 8(f), no intensity was measured in disk 3, whereas for resonance 5 in Fig. 8(g), no intensity was obtained from disk 2. The simulations show good agreement for resonance 5, but deviate a little for resonance 4. The unobserved intensity in disk 3 is not well reproduced (it is lower than in disks 1 and 2, but not zero), which indicates the strong sensitivity on the exact parameters. The fully symmetric mode of the system is resonance 6 that shows intensity in all three disks, and gaps in measurement as well as in the simulation. The measured maps show weak contrast, which is due to a degradation of the SNOM tip. After many scans made to map the modes of the presented samples, the tip loses sharpness, which results in reduced contrast of the measurements. Nevertheless, all modes were identified from their mode maps in agreement with the simulations.

VI. SUMMARY

In summary, we have implemented an experimental method for high-resolution near-field mapping of whispering-gallery modes in coupled disk microresonators using the perturbation of the transmission and reflection signals in a coupled taper-disk system by a scattering SNOM tip. Using a combination of a rigorous modal expansion method with a coupled-mode model, we were able to simulate the transmission and reflection signals measured at both tapered fiber ends. The introduced model is capable of predicting the characteristics observed in the scattering SNOM mode maps. Moreover, we presented detailed mode mappings of two and three coupled microdisks, which are in excellent agreement with theoretical calculations. The obtained information from spectrum measurements and the respective mode intensity distributions can be used, on the one hand, to identify size variations of the individual disks in the fabricated coupled disk samples and, on the other hand, to selectively excite or tune the resonances of such a coupled resonator system. In particular, the samples consisting of three coupled disks can be of interest for sensing applications because it is possible to spatially resolve perturbations of the system (e.g., induced by nanoparticles) due to the fact that depending on its position, only certain modes are influenced. Also it is possible to selectively tune the spectral distance of the modes, e.g., by changing the temperature of a certain disk in the coupled ensemble, which might be useful for optical filter applications.

In spite of the shown agreement between measurements and simulation, the accuracy of the model can be enhanced further by taking into account the real shape of the SNOM tip and describing its interaction with the disk mode beyond the dipole approximation. In order to improve the experimental setup, it is possible to add an interferometric detection scheme, which would allow us to obtain phase information of the measured mode maps.

ACKNOWLEDGMENTS

Parts of this work were funded by the Deutsche Forschungsgemeinschaft (research unit 532 project C) and the German Federal Ministry for Education and Research (Unternehmen Region, ZIK ultra optics).

---

[1] K. Vahala, Nature (London) **424**, 839 (2003).

[2] A. B. Matsko, A. Savchenkov, D. Strekalov, V. S. Ilchenko, and L. Maleki, IPN Progress Report, 42–162, 2005.

[3] A. Naweed, G. Farca, S. I. Shopova, and A. T. Rosenberger, Phys. Rev. A **71**, 043804 (2005).

[4] K. Totsuka, N. Kobayashi, and M. Tomita, Phys. Rev. Lett. **98**, 213904 (2007).

[5] I S. Grudinin and K. J. Vahala, Opt. Express **17**, 14088 (2009).

[6] C. Schmidt, A. Chipouline, T. Käsebier, E. B. Kley, A. Tünnermann, and T. Pertsch, Appl. Phys. B **104**, 503 (2011).

[7] A. Yariv, Y. Xu, R. Lee, and A. Scherer, Opt. Lett. **24**, 711 (1999).

[8] J. Poon, J. Scheuer, Y. Xu, and A. Yariv, J. Opt. Soc. Am. B **21**, 1665 (2004).

[9] A. B. Matsko, A. Savchenkov, D. Strekalov, V. S. Ilchenko, and L. Maleki, IEEE Photonics Technol. Lett. **17**, 136 (2005).

[10] M. A. Popovic, T. Barwicz, M. R. Watts, P. T. Rakich, L. Socci, E P. Ippen, F. X. Kärtner, and H. I. Smith, Opt. Lett. **31**, 2571 (2006).

[11] S. V. Boriskina, Opt. Lett. **31**, 338 (2006).

[12] S. Boriskina, J. Opt. Soc. Am. B **23**, 1565 (2006).

[13] A. Nakagawa, S. Ishii, and T. Baba, Appl. Phys. Lett. **86**, 041112 (2005).

[14] E. I. Smotrova, A. I. Nosich, T. M. Benson, and P. Sewell, Opt. Lett. **31**, 921 (2006).

[15] J. Zhu, S. K. Ozdemir, Y. F. Xiao, L. Li, L. He, D. R. Chen, and L. Yang, Nature Photon. **4**, 46 (2009).

[16] J. T. Robinson, S. F. Preble, and M. Lipson, Opt. Express **14**, 10588 (2006).

[17] W. C. L. Hopman, K. O. van der Werf, A. J. F. Hollink, W. Bogaerts, V. Subramaniam, and R. M. de Ridder, Opt. Express **14**, 8745 (2006).

[18] C. Schmidt, A. Chipouline, T. Käsebier, E. B. Kley, A. Tünnermann, T. Pertsch, V. Shuvayev, and L. I. Deych, Phys. Rev. A **80**, 043841 (2009).

[19] T. Carmon, H. G. L. Schwefel, L. Yang, M. Oxborrow, A. D. Stone, and K. J. Vahala, Phys. Rev. Lett. **100**, 103905 (2008).

[20] M. L. M. Balistreri, D. J. W. Klunder, F. C. Blom, A. Driessen, H. W. J. M. Hoekstra, J. P. Korterik, L. Kuipers, and N. F. van Hulst, Opt. Lett. **24**, 1829 (1999).

[21] S. Blaize, F. Gesuele, I. Stefanon, A. Bruyant, G. Lérondel, P. Royer, B. Martin, A. Morand, P. Benech, and J. M. Fedeli, Opt. Lett. **35**, 3168 (2010).

[22] H. A. Haus, *Waves and Fields in Optoelectronics* (Prentice Hall, New York, 1984).

[23] A. Mazzei, S. Götzinger, L. deS. Menezes, G. Zumofen, O. Benson, and V. Sandoghdar, Phys. Rev. Lett. **99**, 173603 (2007).

[24] C. Schmidt, A. Chipouline, T. Käsebier, E. B. Kley, A. Tünnermann, and T. Pertsch, Opt. Lett. **35**, 3351 (2010).

[25] M. Hammer, J. Opt. Soc. Am. B **27**, 2237 (2010).

[26] M. L. Gorodetsky and V. S. Ilchenko, J. Opt. Soc. Am. B **16**, 147 (1999).

[27] J. D. Jackson, *Classical Electrodynamics* (Wiley, New York, 1975).

[28] E. D. Palik, *Handbook of Optical Constants of Solids* (Academic, New York, 1991).